ACS APPLIED MATERIALS & INTERFACES

Research Article

www.acsami.org

Three-Dimensional Self-Assembly of Networked Branched TiO_2 Nanocrystal Scaffolds for Efficient Room-Temperature Processed Depleted Bulk Heterojunction Solar Cells

Anna Loiudice,[†] Giulia Grancini,[‡] Antonietta Taurino,[§] Michela Corricelli,[∥,⊥] Maria R. Belviso,[#] Marinella Striccoli,[⊥] Angela Agostiano,[∥,⊥] M. Lucia Curri,[⊥] Annamaria Petrozza,[‡] P. Davide Cozzoli,[#,▽] Aurora Rizzo,*[,†,#] and Giuseppe Gigli[†,#,▽]

[†]CBN - Center for Biomolecular Nanotechnologies - Italian Institute of Technology - Energy Platform - Via Barsanti sn, 73010 Arnesano (Lecce), Italy

[‡]Center for Nano Science and Technology @ PoliMi, Istituto Italiano di Tecnologia, Via Pascoli 70/3, 20133 Milano, Italy

[§]IMM CNR-Istituto per la Microelettronica e i Microsistemi, via per Monteroni, 73100 Lecce, Italy

[∥]Dipartimento di Chimica, Università di Bari, Via Orabona 4, I-70126 Bari, Italy

[⊥]Istituto per i Processi Chimico Fisici (IPCF-CNR) Bari, c/o Department of Chemistry, Via Orabona 4, I-70126 Bari, Italy

[#]National Nanotechnology Laboratory (NNL), CNR-Istituto Nanoscienze, c/o Distretto Tecnologico, via per Arnesano km 5, 73100 Lecce, Italy

[▽]Dipartimento di Matematica e Fisica "E. De Giorgi", Università del Salento, via Arnesano, 73100 Lecce, Italy

Supporting Information

ABSTRACT: In this work, we report on ~4% power conversion efficiency (PCE) depleted bulk heterojunction (DBH) solar cells based on a high-quality electrode with a three-dimensional nanoscale architecture purposely designed so as to maximize light absorption and charge collection. The newly conceived architecture comprises a mesoporous electron-collecting film made of networked anisotropic metal-oxide nanostructures, which accommodates visible-to-infrared light harvesting quantum dots within the recessed regions of its volume. The three-dimensional electrodes were self-assembled by spin-coating a solution of colloidal branched anatase TiO_2 NCs (BNC), followed by photocatalytic removal of the native organic capping from their surface by a mild UV-light treatment and filling with small PbS NCs via infiltration. The PCE ~ 4% of our TiO_2 BNC/PbS QD DBH solar cell features an enhancement of 84% over the performance obtained for a planar device fabricated under the same conditions. Overall, the DBH device fabrication procedure is entirely carried out under mild processing conditions at room temperature, thus holding promise for low-cost and large-scale manufacturing.

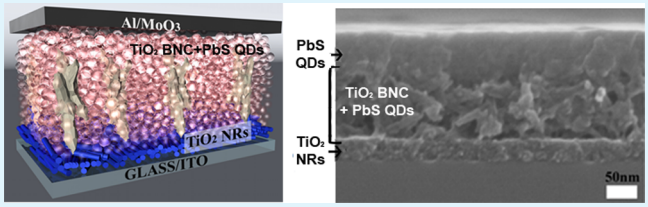

KEYWORDS: *bottom up, nanocrystal, depleted bulk heterojunction, solution-processed photovoltaics*

INTRODUCTION

Photovoltaic (PV) technology is a highly attractive process for supplying clean and renewable energy.[1,2] The growing demand for PV alternatives has stimulated intensive research efforts toward the so-called third-generation organic[3−5] and dye-sensitized solar cells,[6,7] which promise to perform solar energy conversion at lower cost than well-established technologies. In the search for high-efficiency and cost-effective solar cell solutions, nanostructured materials have also drawn much interest.[8,9] Among these, colloidal semiconductor nanocrystals (NCs) offer many opportunities in the assembly of nanoscale devices and arrays by the bottom-up paradigm[10−12] and, most notably, allow attributing enhanced or novel functions crucial to the design of advanced optoelectronic devices. Essential to realizing their PV applications through the bottom-up approach is the rational control of the key NC parameters, including chemical composition,[13] crystal structure,[14] size,[15] morphology,[16] and surface ligands,[17] which determine the ultimate electronic and optoelectronic properties critical to predictable device functioning.

Novel device architectures based on solution-processable colloidal NCs and nanostructured interfaces at the electron-extracting electrode can enable improved photocurrent by allowing a higher overall light absorption.[18−20] This has been demonstrated using ZnO nanowires[19] or large TiO_2 nanostructured electron-accepting templates[20] infiltrated with PbS quantum dots (QDs) in devices known as depleted bulk heterojunction (DBH) solar cells, analogous to their bulk

Received: January 7, 2014
Accepted: March 7, 2014
Published: March 7, 2014

   dx.doi.org/10.1021/am500110x | ACS Appl. Mater. Interfaces 2014, 6, 5026−5033

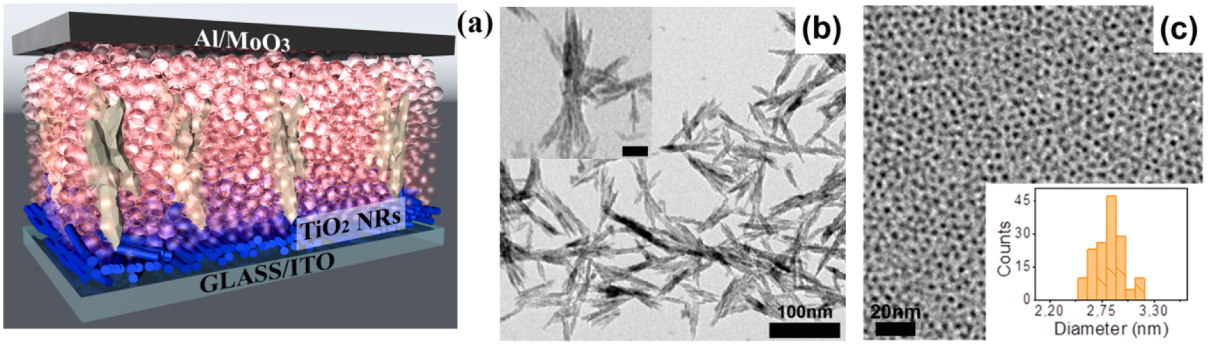

Figure 1. (a) Sketch of the DBH device. (b) TEM micrograph of the as-synthesized TiO_2 BNCs (inset is a magnified mage of a single BNC (scale bar = 20 nm)) and (c) of the as-synthesized PbS QDs with the corresponding size distribution (inset).

heterojunctions (BHJ) widely employed in PV polymer devices.[21,22] In such PV cells, a three-dimensional-configured electron-acceptor film allows a larger volume of QD sensitizers to be incorporated, which naturally guarantees a blend of satisfactory light-harvesting and efficient charge-collection properties, otherwise difficult to achieve at once in conventional devices based on p−n junction bilayers.[23,24]

There is still much scope for further improvement in device structure through engineering electrodes with high electron mobility, based, for example, on nanopillars, nanowires, and nanopores, by means of mild low-temperature, solution-based processes. In fact, all attempts made so far to address these challenges have relied on the development of ZnO or TiO_2 electrodes via procedures that involve a thermal annealing step at temperatures of ∼400−500 °C either to generate the desired nanowire structures[20] or to convert an initial sol−gel derived nonstoichiometric amorphous metal-oxide from into a crystalline stoichiometric phase and remove any associated organic components.[19] Such fabrication approaches severely limit substrate choice and monolithic multijunction device architectures.

In this paper, we report on a room-temperature, solution-processed infrared-bandgap DBH solar cell that relies on a three-dimensional (3D) electron-acceptor thin-film layer obtained upon self-assembly of preformed colloidal branched anatase TiO_2 NCs (BNCs). The processing under mild conditions guarantees that the TiO_2 BNCs retain their crystal phase and geometry, leading to a uniform 3D thin-film architecture characterized by a mesoporous nanostructure with effective inter-BNC connectivity. After deposition, the native insulating hydrophobic surfactants bound to the surface of the BNCs are removed by exploiting UV light-driven photocatalytic demolition.[25,26] The resulting 3D network of BNCs allows accommodation of a large volume fraction of light-sensitizer PbS QDs into the nanoscale voids intervening within the mesoporous TiO_2 films via facile infiltration. As a result, light harvesting in the vis−near IR region is maximized, and concomitantly, electron diffusion is facilitated by the extended heterointerface holding between TiO_2 BNCs and PbS QDs. Development and optimization of large-interfacial-area solar cells based on the above NC-based DBH device design have been guided by a careful study of the charge-separating interface between the electron accepting and donating phases. A complete investigation on the role of materials processing parameters and their influence on the ultimate PV performance of the DBH solar cells has been carried out.

For an optimal solar cell configuration, we demonstrate a record photon energy conversion efficiency (PCE) of 3.9% under simulated AM1.5 illumination, which is, to the best of our knowledge, among the highest NC-based DBH solar cell efficiency ever documented for devices fabricated under room-temperature conditions. Our DBH structure demonstrates an overall 2-fold improvement in PCE compared to a p−n junction bilayer made under the same conditions. Moreover, a fundamental study of the photoinduced charge carrier dynamics, performed by nanosecond transient absorption spectroscopy measurements, reveals that the DBH structure achieves efficient charge separation and transport due to an increase in the carrier lifetime.

RESULTS AND DISCUSSION

Our DHB device structure (see Figure 1a) consists of a sandwich of (i) a flat and dense buffer layer of colloidal TiO_2 nanorods (NRs) spin-coated onto an indium tin oxide (ITO) electrode and (ii) a 3D-networked TiO_2 BNC mesoporous film backfilled with PbS QDs via infiltration. The PbS QDs exhibit a broad absorption over the entire solar spectrum and allow the solar cell sensitivity to be extended to the infrared radiation. Upon absorption, charge separation occurs at the extended interface between the PbS QDs and n-type TiO_2 within the BNC-made mesoporous film.

TiO_2 BNC Film Fabrication. Colloidal anatase TiO_2 BNCs were synthesized by a surfactant-assisted nonaqueous sol−gel route based on sequential aminolysis and pyrolysis reaction of titanium oleate complexes, which take place upon high-temperature processing of $TiCl_4$/oleic acid/oleyl amine/octadecene mixtures under an inert atmosphere.[27] In this approach, the surfactants play the multiple roles of reactants (oleic acid serves as oxygen atom source, while oleyl amine acts as nucleophile driving the aminolytic decomposition), reactivity moderators, and surface stabilizers preventing irreversible coalescence during growth. After synthesis and purification, the BNCs are easily redispersible in nonpolar organic media for subsequent solution-processing, due to the robust hydrophobic shell of oleate anions bound to their surface.[27] Figure 1b reports a representative transmission electron microscopy (TEM) image of the TiO_2 BNCs used in this work. Individual BNCs are made of a bunch of multiple nanorod arms (3−4 nm in diameter, 80−100 nm in length) that appear to have been tied at their median region and fanned out at their extremities in a sheaf-like configuration. The BNCs are single-crystalline tetragonal-phase anatase nanostructures, composed of [001]-elongated arms departing out of the central branch region. A detailed characterization of the structural properties of the BNCs can be found elsewhere.[27]

The BNCs were used as building blocks to construct thin films that should function as the electron-acceptor layers in the designed DBH solar cell. Due to their particular open-split skeleton with double-fantail morphology, such BNCs can be expected to be assembled into 3D mesoporous architecture allowing a significant volume fraction of nanoscale voids for the incorporation of QD sensitizers of suitable size.

In the electron-acceptor layer fabrication process, a major challenge concerns the placement of the NCs within the active device structure and the preservation of their original structural and geometric features. Most current approaches devised to assemble 2D and 3D NC superlattices on solid substrates rely on time-consuming colloidal crystallization techniques that require NCs with monodisperse sizes and shapes and precise control of interparticle interactions.[28,29] The application of such procedures to construction of NC assemblies in a device structure remains inherently prohibitive. For a successful integration of self-assembled BNCs into our working device, the key step required was represented by the formulation of an appropriate spin-coating solution. Indeed, uncontrolled interparticle aggregation phenomena that commonly occur during NC solution preparation could have dramatic effects on the ultimate energy conversion efficiency of a solar cell.

To reproduce the same conditions as those used for our device fabrication, the optimization of the TiO_2 BNC layer deposition process was carried out on a dense and flat buffer layer made of small (3−4 nm × 20 nm) anatase TiO_2 NRs, which was assembled as reported earlier[25,26] (see Methods for details). The concentration of BNCs and the solvent of the spin-casting solution were tuned, with predictable effects on the resulting mesoporous layer, as illustrated in Figure 2a,b. Upon depositing a diluted chloroform solution of the as-synthesized TiO_2 BNCs, the BNCs pile up into 3D island-like stacks, leaving large regions of the TiO_2 NRs underlayer uncovered (Figure 2a). For very low BNC concentrations (Figure 2b), a countable number of BNCs distributed homogeneously on the TiO_2 NRs underlay is obtained. The BNCs can be imaged individually, or in close-packed groups of a few individuals (see inset in Figure 2b).

On changing the solvent from chloroform to toluene (Figure 2c) or α-terpineol (Figure 2d), the deposited films still entail BNCs assembled into 3D stacks. In all of these cases, although the initial BNC coverage of the buffer layer stays high, regions characterized by BNC multilayers occurred frequently, with the total area of intervening "voids" staying approximately constant, regardless of dispersing solvent used. This fact suggests that the BNCs may tend to form aggregates already in solution or during solvent evaporation, due to strong interparticle attractions. Therefore, further attempts to pursue uniform BNC layers starting from exceedingly diluted suspensions were considered to be useless. For the purposes of this work, we have not studied such multilayer structures, but instead we have focused on the more controllable process of generating ordered nanostructured BNC monolayer and submonolayer coverage suitable for device fabrication.

In order to facilitate screening of interparticle attractions and promote BNC deposition into uniform films conformal to the NRs buffer substrate, we have devised a simple approach for the formulation of the spin-coating precursor solution, reminiscent of the technique exploited to prepare screen-printable TiO_2 BNC pastes suitable for fabricating mesoporous oxide photoelectrodes for dye-sensitized solar cells.[30] Our strategy allows one to simultaneously adjust the miscibility of the BNCs in their dispersing solvent and improve their colloidal stability by using α-terpineol as both a regulator of medium polarity and viscosity and a surface binding agent. The technique by which the BNCs/α-terpineol mixture is prepared is critical to guaranteeing optimal results. Our procedure involves performing the slow calibrated addition of a chloroform solution of the as-synthesized BNCs to α-terpineol under vigorous stirring (see Methods). Such a particular sequence of combining BNCs and α-terpineol facilitates disruption of the original BNC aggregates and subsequent maximization of interactions between the hosting medium and the as-deassembled BNCs. This mechanism ensures efficient kinetic stabilization of the BNCs that are gradually liberated, thus depressing the tendency toward recoagulation (which otherwise dominates when an exceedingly high concentration of BNCs is present during the course of BNC/α-terpineol mixing). SEM inspection at variable magnification of films spin-casted from the as-prepared BNC/α-terpineol solution on the TiO_2 NRs buffer layer (Figure 2e,f) reveals formation of a continuous spongy network of individually distinguishable nanoscale building blocks, which are interconnected through small junction points at random

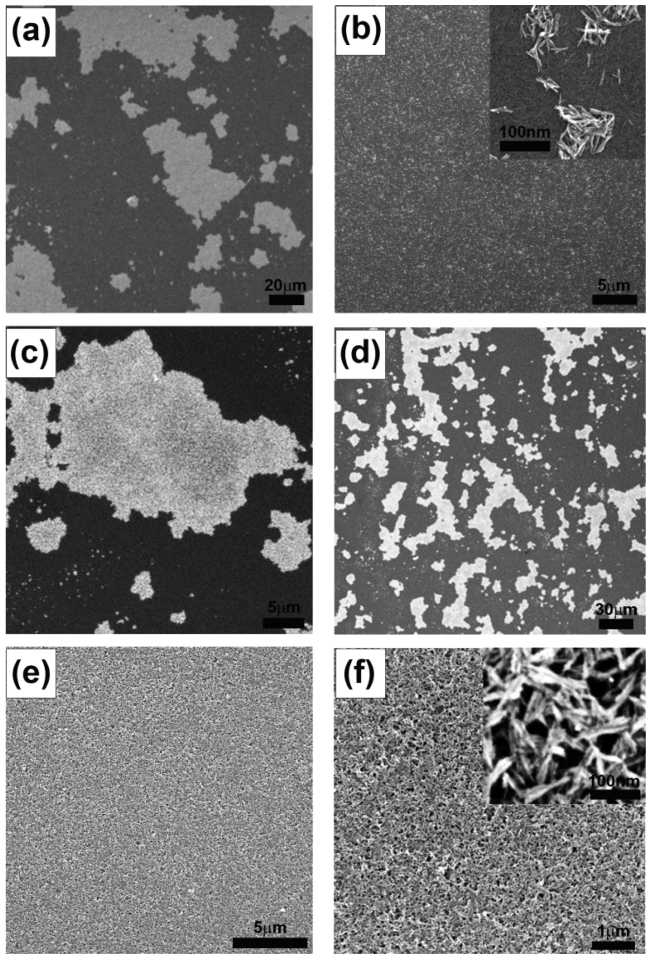

Figure 2. Top-view SEM images of UV-treated TiO_2 BNC films deposited onto a flat layer of TiO_2 NRs. The as-synthesized TiO_2 BNCs were diluted at different concentrations before the deposition: (a) 1.1 mM in chloroform (1:1 v/v), (b) 0.3 mM in chloroform (1:6 v/v), (c) 1.1 mM in toluene (1:1 v/v), (d) 1.1 mM in α-terpineol (1:1 v/v). (e and f) 1.1 mM in α-terpineol obtained by adding incremental aliquots of the as-synthesized BNCs in α-terpineol until reaching the desired concentration.

dx.doi.org/10.1021/am500110x | ACS Appl. Mater. Interfaces 2014, 6, 5026−5033

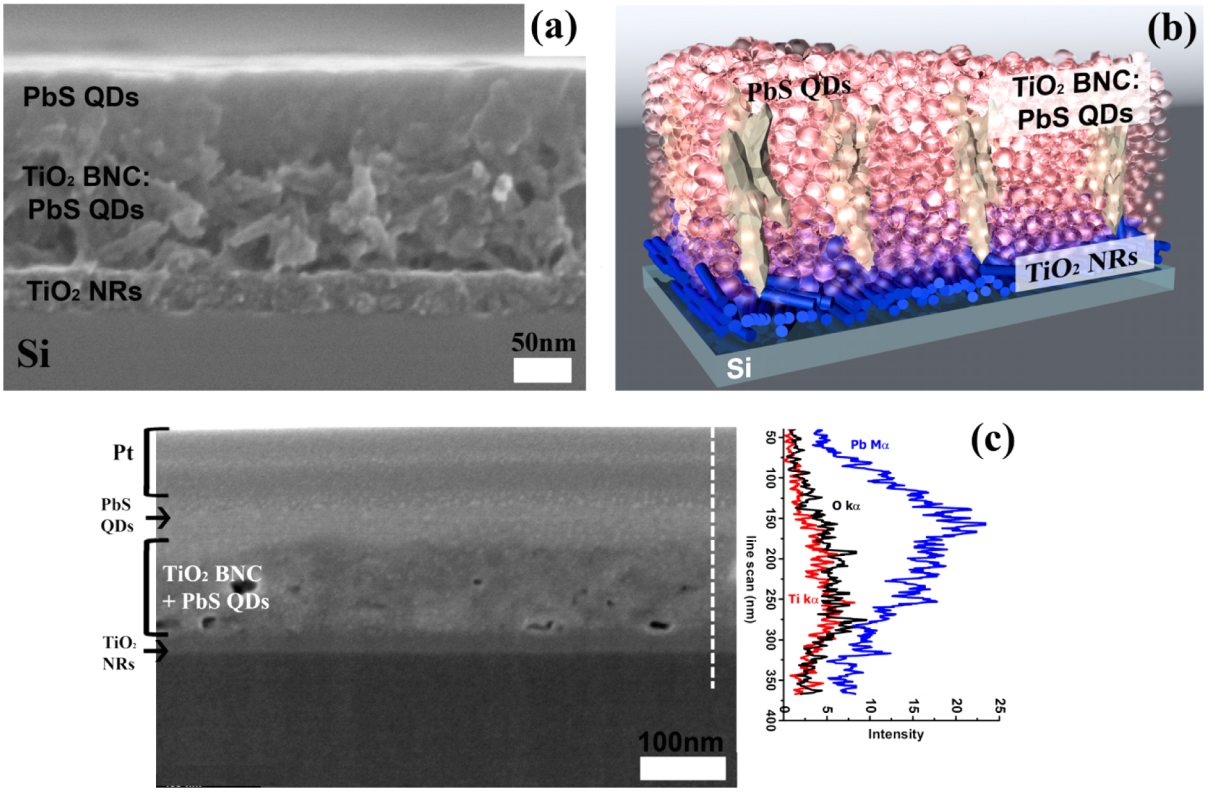

Figure 3. (a) Cross-section SEM image of the TiO_2 NRs/TiO_2 BNC/PbS QDs DBH on the Si/SiO_2 substrate and (b) sketch of the corresponding DBH layer. (c) SEM image of a polished section of the BHJ (left) along with a corresponding EDS line scan profile (right) showing the Pb Mα Ti Kα and O Kα signals acquired along the dashed white line marked on the SEM picture.

locations and hence appear to be accommodated in different relative orientations relative to the substrate underneath. Interestingly, such identified units possessed dimensional and morphological features closely resembling those of the starting BNCs. Further demonstration is given by the atomic force microscopy (AFM) topography and phase images (Figure S1 in the Supporting Information (SI)).

The oleate ligands bound to the BNC surface, and whenever used, the α-terpineol additive molecules were eliminated by exposing the film to a cw-UV lamp at room temperature in the air. The UV-treated TiO_2 BNC films were examined by FT-IR, which showed the suppression of the stretching vibrations of the C−H moieties of the alkyl chain signals, thus proving the effective removal of the surface ligands (Figure S2, SI).[25,26]

By means of the procedures for TiO_2 BNC film deposition described above, three main advantages, relevant to DBH device fabrication and operation, can be achieved. First, the conductivity of the BNC films is increased by eliminating the potential barrier caused by the original insulating native ligands and any other contaminating organic components. Second, a 3D nanostructured mesoporous film with regular thickness and homogeneous texture without any detectable micrometer size aggregates and cracks over areas of several square micrometers is obtained. Third, the overall fabrications approach allows fabrication of robust electrodes at room temperature, thus bypassing the harsh sintering treatments that are instead required to create conductive electron-extracting oxide films by conventional approaches.[19,20]

Device Operation and Performance. Small TiO_2 NRs (3 × 20 nm) were spin coated on the indium−tin oxide (ITO) substrate to create a close-packed layer (40 nm) that could not be penetrated by the PbS QDs, hence preventing shunting between the PbS QDs and ITO. The elongated structure of NR shaped TiO_2 leads to a more efficient charge transport with respect to the spherical one.[31] The second layer of TiO_2 BNCs, which was deposited as described above, represents the 3D nanostructured electrode of our DBH device. The thickness of this layer corresponds to the length of a single BNC (~150 nm), that is, the maximum thickness achievable with one deposition step. The formation of a BNC monolayer guarantees an optimal pore size to ensure a complete infiltration of PbS QDs. The deposition of additional BNC layers to obtain a thicker scaffold will result in a reduction of the pore size to the detriment of PbS QDs infiltration. To sensitize the BNC TiO_2 layer, we used PbS QDs with a narrow size distribution of 2.8 ± 0.5 nm, as demonstrated by the TEM micrograph and relative size histogram in Figure 1b. The absorption spectrum of a toluene solution of the PbS QDs in Figure S3 displays a well-resolved exciton transition signal, centered at 871 nm, in agreement with the QD size regime and monodispersity. The corresponding photoluminescence (PL) spectrum is characterized by a single narrow emission band, Stokes-shifted by 124 nm with respect to the corresponding exciton absorption peak, which originates from band-edge recombination. No signal can be ascribed to defect states.

The PbS QDs were deposited layer-by-layer on the electrode until an optimal thickness had been reached. During this process, the QDs intercalated within the voids of the networked BNCs, approaching a limiting filled volume fraction beyond which excess QDs started to accumulate on the top of the BNC film. To avoid direct contact between the top ohmic contact and the TiO_2 BNCs, the overall thickness of such a 3D PbS/

dx.doi.org/10.1021/am500110x | ACS Appl. Mater. Interfaces 2014, 6, 5026−5033

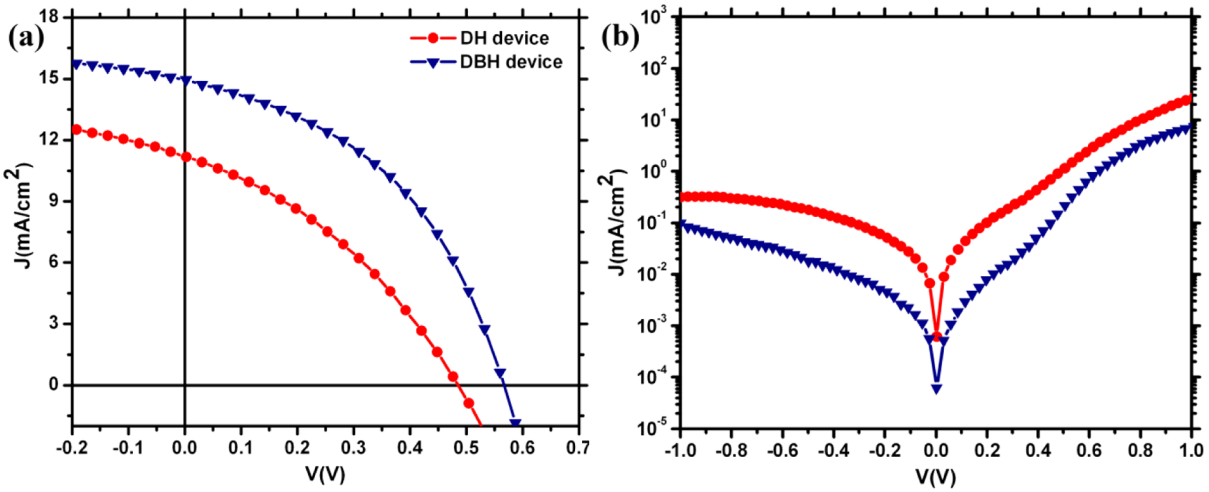

Figure 4. Current density vs applied bias (J–V) characteristics under AM1.5 G (100 mW cm^{-2}) simulated solar illumination (a) and in the dark (b) for the DH and DBH based solar cell.

TiO_2 bulk heterojunction was set so as to slightly exceed (~180 nm) the thickness of the mesoporous BNC layer (~150 nm). Figure 3a shows a cross-sectional SEM image of the fabricated device, obtained from a cleaved edge of the sample. The image clearly shows the sequence of layers forming the device, i.e., the TiO_2 NRs, the TiO_2 BNC, and the PbS QD layers, respectively. The sketch of the DBH architecture is depicted in Figure 3b.

While a quite sharp interface separates the TiO_2 NRs layer from the TiO_2 BNC layer, no sharp transition is visible between the TiO_2 BNC and the topmost PbS QDs layer. This suggests that the PbS QDs could actually have intercalated within the TiO_2 BNC layer through the recessed pores naturally accommodated within the network of interconnected TiO_2 BNCs. To confirm this picture, the compositional profile of the DBH layer across the PbS QD/TiO_2 BNC interface was assessed by spatially resolved energy-dispersive X-ray spectroscopy (EDS) analyses. EDS line scan profiles were collected on a finely polished section, obtained by ion milling after the deposition of a protective Pt strip on the PbS QD surface. The analyses were performed at high resolution, in order to map the distribution of chemical elements on a nanometer length scale. Figure 3c reports a SEM image of a polished cross-section of the DBH, where the topmost Pt strip and the other layers of the device are evident. It is worth noting that the section preparation procedure enhanced the contrast of the image, thus allowing the visibility of the PbS QDs in some areas of the TiO_2 BNC layer. The Pb Mα, Ti Kα and O Kα signals acquired along the direction of the electron beam scan are shown on the right side panel of the SEM image. The spatial profile of the Pb signal intensity evidences a sharp asymmetry: it initially increases with the distance from the top surface of the cross-section, reaching a maximum at about 180 nm; then it slowly decreases to the background level deeply across the subsequent 150 nm, where the Ti and O signals authenticate the presence of the assembled BNCs. This feature confirmed that the PbS QDs had actually diffused into the underlying TiO_2 BNC layer, with excess QDs having accumulated on top of it. Further proof of the presence of PbS in the TiO_2 BNC layer was provided by suitable FIB milling experiments (see Figure S4, SI). A rectangular dig was milled by ion beam on the surface of the cross-section in order to completely remove the PbS layer. Successively, EDS spectra were acquired from areas at the bottom of the dig (where only the TiO_2 BNC layer was present—see Figure S4a) and in the PbS layer, in a region nearby the dig (Figure S4 b). The corresponding spectra (Figure S4c) confirmed the presence of Pb and S in both analyzed regions of the cross-section.

The benefits of using a TiO_2 BNC layer for solar cells are demonstrated in Figure 4 and Table 1. For comparison purposes, we fabricated a corresponding bilayer device, namely a depleted heterojunction (DH) device, made of a TiO_2 NRs layer (~150 nm) interfaced with a PbS QDs layer with the same overall thickness as that realized in the DBH device (~180 nm), while keeping other fabrication parameters fixed. The current–voltage (I–V) characteristics of the devices under AM1.5G simulated intensity and in the dark (Figure 4a and b, respectively—see Table 1) indicate that the DBH device yields a short-circuit current density (J_{SC}) in excess of 15.0 mAcm^{-2} and a higher FF and V_{OC}. The best-performing DBH device can achieve a PCE as high as 3.9% (with an almost 100% improvement of efficiency over the DH device), which is among the best performance ever reported for the solar cells entirely fabricated at room temperature.

Table 1. Photovoltaic Parameters for DH and DBH Solar Cells

device	PCE (%)	FF	V_{oc} (V)	J_{sc} (mA/cm^2)	R_{sh} (Ω cm^{-2})
DH	2.10	0.36	0.49	11.55	3.9×10^3
DBH	3.87	0.45	0.57	14.98	5.2×10^4

Dark I–V data were examined to gain further insight into the contribution of the TiO_2 BNC in this architecture. A fit of the forward diode current to the linear regime reveals that the introduction of the BNC interfacial layer leads to a 100 mV shift in this onset. The improved onset of the dark forward current implies a reduction in carrier recombination through an improved interface. Normally, the V_{OC} of devices with a bilayer structure is higher than that of BHJ solar cells because fewer continuous pathways may act as shorting channels between top and back electrodes in these devices. Differently, as shown by the SEM cross-section of Figure 3b, our DBH architecture is characterized by the presence of two thin layers of TiO_2 NRs and PbS QDs located near the ITO and MoO_3 electrodes, respectively, which alleviate the shorting drawback, thus reducing the extent of recombination processes. The shunting

dx.doi.org/10.1021/am500110x | ACS Appl. Mater. Interfaces 2014, 6, 5026–5033

resistance (R_{sh}) is an important factor to evaluate the leakage current level in a solar cell. In the equivalent-circuit model of an ideal solar cell, the R_{sh} is infinite and represented by a resistor connected in parallel with a diode. In real photovoltaic devices, the shorting current between top and back electrodes reduces R_{sh} to a finite value. The R_{sh}'s of different devices were obtained by calculating the inverse derivative of the dark current at $V = 0$. As listed in Table 1, a higher V_{OC} is ascribed to a larger R_{sh}, indicating a lower leakage current in devices based on BNC films. This is also corroborated by an increase in the FF (Table 1), which implies a higher maximum power point current as a result of delayed turn-on of current injection due to the charge-blocking effect.

For the sake of completeness, we have also analyzed the J–V characteristics and photovoltaic parameters under illumination of the devices fabricated using different TiO_2 BNC films obtained by changing the suspension preparation conditions (Figure S5 and Table S1), described in the previous section. It can be readily observed that the photovoltaic parameters remain unchanged with respect to those of the DH device. This is probably due to the presence of both large voids and big aggregates of TiO_2 BNCs on the TiO_2 NR underlayer that inhibit the PbS QDs infiltration. These results emphasize the importance of the materials processing and how the formation of a continuous spongy network of individually distinguishable nanoscale building blocks is suitable for improving device performance.

To better understand the physical origin of the improved performances of the BNC-based devices, we performed nanosecond transient absorption (nsTA) spectroscopy measurements. For comparison, the nsTA spectral evolution has been carried out for PbS QDs deposited both on NR-only and on BNC-only films. Results are summarized in Figure 5. Figure 5a shows the differential absorption spectra for the two systems integrated over the first 500 ns after pump excitation. The PbS QDs show a positive band peaking around 850 nm, ascribable to the PbS photobleaching (PB) due to the filling of the 1S state, and a negative signal at shorter wavelengths, peaking around 550 nm, arising from photoinduced absorption (PA) from populations of QD surface trap states.[26] The PA band of the PbS QDs deposited on TiO_2 NRs presents a higher intensity, while the PB band of the two systems is comparable. This suggests that, upon photoexcitation, a higher density of trap states is populated in the PbS QDs deposited on TiO_2 NRs, relative to QDs deposited on the BNCs, to the detriment of the percentage of the electrons injected into the TiO_2.

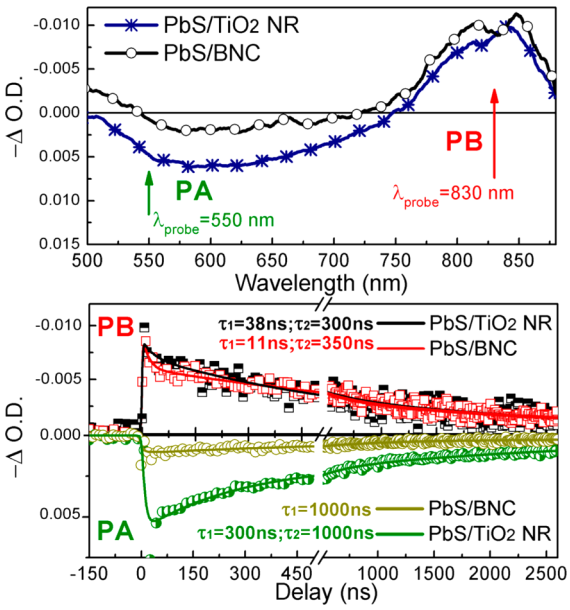

Figure 5. (a) Differential absorption spectra of PbS QDs on TiO_2 BNC and NRs-shaped ones. (b) PB dynamics at 830 nm and PA dynamics at 550 nm probe wavelength in the first 2.5 us time range.

Figure 5b illustrates the decay dynamics of the PB and PA bands. For the PbS QD/BNC system, the monitored PB signal shows a fast initial decay component (fitted with a time constant of around 11 ns) and a longer living tail. The fast initial decay, not observable for the PbS/TiO_2 NR, or for the PbS on glass (see Figure S6 in the SI), may reflect the residual electron transfer from the $1S_e$ level to the TiO_2 conduction band levels. It has indeed been demonstrated[26] that electron injection at this interface occurs via several pathways over a temporal range spanning from 200 fs to the hundreds of picseconds–nanoseconds time scale.

The longer-living component is associated, on the other hand, with electron–hole recombination ($1S_e \rightarrow 1S_h$), as retrieved from the PB decay of the pristine PbS QD film (see Figure S6 in the SI). The PA dynamics is also characterized by a different behavior for the two samples. The PbS QD/NR system exhibits a fast component (300 ns) and a longer living tail, similarly to what was observed for the pristine PbS QD (see Figure S6 in the SI). Thus, we assign the former to the recombination of trap states at the QD surface. Interestingly, the PbS QD/BNC system shows only a residual long-living component, confirming that after photoexcitation, a lower density of population fills the trap states. These features can be directly translated in the observed improved performances of the PbS QD/BNC based-device, which shows both larger V_{OC} and higher photocurrent.

CONCLUSIONS

In summary, we have developed a solution-processing approach for the bottom-up fabrication of a TiO_2 thin-film electrode made of 3D-networked colloidal BNCs, which features a mesoporous structure, with regular thickness and homogeneous texture without any detectable micrometer-size aggregates or cracks. The long-chain insulating ligands attached to the as-synthesized TiO_2 BNC are removed by means of a room-temperature UV treatment in air. We have built a DBH solar cell in which the newly developed BNC thin-film electrode works as a 3D-configured acceptor of electrons transferred from phoexcited infrared-to-visible light absorbing PbS QDs infiltrated within the BNC network. These TiO_2 BNC/PbS QD DBH solar cells allow the achievement of improved FF, V_{OC}, and J_{SC} and a PCE of ~3.9%, featuring an almost 100% enhancement over the performance obtained for a planar device fabricated under the same conditions. The use of room-temperature processing approaches for their fabrication renders these new DBH QD solar cells compatible with flexible substrates and multijunction device architectures, which could pave the way to a further step increase in solar cell efficiency.

METHODS

Preparation of BNC Solutions for Thin-Film Deposition by Spin-Coating. A 20 μL aliquot of a colloidal solution of the as-synthesized (purified) BNCs dispersed in chloroform was slowly added (1 μL/min) to 1 mL of pure α-terpineol, under vigorous

dx.doi.org/10.1021/am500110x | ACS Appl. Mater. Interfaces 2014, 6, 5026–5033

magnetic stirring until a concentration of 1.1 mM was reached. The final solution was stirred at room temperature for 12 h.

Device Fabrication. During device fabrication, a thin blocking layer of compact TiO_2 was first deposited by spin coating the anatase TiO_2 NRs solution onto a prepatterned ITO glass substrate.[25,26] Subsequently, a TiO_2 BNC layer was deposited by spin coating the anatase TiO_2 BNCs suspension (700 rpm for 60 s), resulting in a TiO_2 BNC film with a thickness of 150 nm. Both the blocking layer and the mesoporous layer were treated with a continuous-wave-UV (cw-UV) lamp, as reported in our previous work, in order to remove completely the insulating surfactants.[25,26] The procedure for the deposition of the PbS QD film is similar to the one reported by Sargent et al.[15] with modifications. The PbS QDs were subsequently deposited layer by layer on the porous TiO_2 film by spin coating a 50 mg·mL^{-1} solution in octane. Each layer was cast at a spinning rate of 2500 rpm for 10 s and thereafter briefly treated with a solution of 0.2% v/v 3-mercaptopropionic acid (MPA, ≥ 99.0% from Sigma-Aldrich) in methanol using again 2500 rpm rotational speed for 10 s. This treatment completely displaced the oleate ligand and rendered the QDs insoluble, which allowed thin films of 150 nm thicknesses to be created using seven successive deposition cycles. Each layer was rinsed with anhydrous methanol and octane (purchased from Sigma-Aldrich) to remove the excess of MPA and PbS QDs. Finally, a MoO_3/Al back contact of ∼10 nm/100 nm thickness was deposited by evaporation through a shadow mask.

Characterization Technique. *Vis–NIR Absorption and Photoluminescence Emission Spectroscopic Analysis.* For vis–NIR absorption measurements, a Cary Varian 5000 UV–visible–NIR spectrophotometer was used. PL emission measurements were performed with a Horiba Jobin Yvon Fluorolog-3 spectrofluorimeter, using a 450 Xe lamp as the excitation source, coupled to a double grating Czerny-Turner monochromator for wavelength selection. The detection system is constituted of a TBX-PS detector in the visible range and a Peltier-cooled InGaAs detector in the NIR range.

TEM Analysis. TEM analyses were performed by using a Jeol Jem-1011 microscope, working at an accelerating voltage of 100 kV. TEM images were acquired by a Quemesa Olympus CCD 11 Mp Camera. The samples were prepared by dipping the 300 mesh amorphous carbon-coated Cu grid in toluene solution of PbS QDs. Size statistical analysis (NP average size and size distribution) of the samples was performed by means of freeware ImageJ analysis program.

SEM and EDS Analysis. A Zeiss NVISION 40 dual beam Focused Ion Beam (FIB) machine, equipped with a high resolution SEM Gemini column and an Oxford 350 x-act EDS spectrometer, was used for SEM and EDS experiments. Morphological and chemical investigations were carried out in cross-sectional geometry, both on a cleaved edge of the device and on ad-hoc prepared sections. The sections were prepared in situ by ion milling: a protective Pt strip was electron-deposited on the surface of the sample, very close to one cleaved edge of the device; then a rectangular dig was milled and the section carefully polished in order to enhance the visibility of the layers. Once the polishing procedure had been completed, the sample was tilted away from the FIB configuration (sample surface perpendicular to the ion beam and at 54° with respect to the electron beam) and investigated by SEM and EDS with the section perpendicular to the electron beam.

Nanosecond Transient Absorption. Nanosecond transient absorption measurements were carried out with an LP920 laser flash spectrometer (Edinburgh Instruments) based on a standard transient absorption setup, where the sample is excited by a nanosecond laser pulse, and the time evolution of the differential absorption changes induced by the pump is monitored by a cw light source probe. The pump pulses were provided by a nanosecond tunable OPOLett-355II laser (10 Hz repetition rate). The probe light was provided by a pulsed xenon arc lamp. The sample was kept at a 45° angle to the excitation beam. The beams were focused onto the sample ensuring the spatial overlap. The transmitted probe is spectrally filtered by a monochromator and detected. Two different detection systems are used: a cooled ICCD camera allowing detection of the entire spectral range from 350 to 850 nm at once and a set of photomultipliers (with both vis and near-IR detection window) enabling collecting of the single-wavelength kinetics with higher sensitivity. The signal was finally recorded by a TDS 3032C digital signal analyzer. From the transmission change following photoexcitation, the variation in the absorption was thus derived as

$$\Delta \mathrm{OD}(\tau, \lambda) = \frac{\log(I_{\mathrm{probe}})}{I_{\mathrm{t}}(\tau, \lambda)}$$

where I_{probe} is the transmitted probe with excitation off and I_{t} is the transmitted probe after laser excitation. The system had sensitivity of 5×10^{-4} and a temporal resolution of 7 ns.

■ ASSOCIATED CONTENT

Ⓢ Supporting Information

Detailed list of chemicals used, methods for synthesis and purification of nanocrystals. AFM images and FTIR analysis of TiO_2 BNC films, complete PL spectrum of PbS QDs in solution, SEM image with EDS analysis of the cross-section of the DBH layer after milling, the J–V characteristics of devices fabricated using the different TiO_2 BNC suspensions, and transient absorption dynamic of the PbS QDs deposited on a bare glass substrate. This material is available free of charge via the Internet at http://pubs.acs.org.

■ AUTHOR INFORMATION

Corresponding Author

*Tel.: 0039-0832-298211. Fax: 0039-0832-298237. E-mail: aurora.rizzo@nano.cnr.it.

Notes

The authors declare no competing financial interest.

■ ACKNOWLEDGMENTS

This work has been supported by Dispositivi Solari a Coloranti di Nuova Generazione: Sensibilizzatori e Conduttori Nano-Ingegnerizzati (MIUR-PRIN 2010-2011 Project No. 20104XET32 "DSSCX") Materiali innovativi per il fotovoltaico organico e ibrido (MIUR-PRIN 2009 prot. 2009PRAM8L), EFOR-Energia da FOnti Rinnovabili (Iniziativa CNR per il Mezzogiorno L. 191/2009 art. 2 comma 44), by Research Project PON 2007–2013 (Avviso n. 713/Ric. del 29 ottobre 2010), by MAAT-Molecular Nanotechnology for Health and Environment (Project number: PON02_00563_3316357) and by the EU seventh FP ORION project (CP-IP 229036-2). The authors gratefully acknowledge Dr. Raffaella Buonsanti and Dr. Gian Luca De Gregorio for fruitful discussions and Alberto Mirasola for the help in the 3D graphic design.

■ DEDICATION

This work is dedicated to the memory of Dr. Gianluca Latini, who passed away in March 2012.

■ REFERENCES

(1) Lewis, N. S. Toward Cost-Effective Solar Energy Use. *Science* **2007**, *315*, 798–801.

(2) Ginley, D.; Green, M. A.; Collins, R. Solar Energy Conversion Toward 1 Terawatt. *MRS Bull.* **2008**, *33*, 355–364.

(3) Shaheen, S. E.; Ginley, D. S.; Jabbour, G. E. Organic-Based Photovoltaics: Toward Low-Cost Power Generation. *MRS Bull.* **2005**, *30*, 10–19.

(4) Scharber, M. C.; Sariciftci, N. S. Efficiency of Bulk-Heterojunction Organic Solar Cells. *Prog. Polym. Sci.* **2013**, *38*, 1929–1940.

(5) Gao, F.; Ren, S. Q.; Wang, J. The Renaissance of Hybrid Solar Cells: Progresses, Challenges, and Perspectives. *Energy Environ. Sci.* **2013**, *6*, 2020−2040.
(6) Zhang, S.; Yang, X.; Numataa, Y.; Han, L. Highly Efficient Dye-Sensitized Solar Cells: Progress and Future Challenges. *Energy Environ. Sci.* **2013**, *6*, 1443−1464.
(7) Grätzel, M. Dye-Sensitized Solid-State Heterojunction. Solar Cells. *MRS Bull.* **2005**, *30*, 23−28.
(8) Beard, M. C.; Luther, J. M.; Semonin, O. E.; Nozik, J. A. Third Generation Photovoltaics Based on Multiple Exciton Generation in Quantum Confined Semiconductors. *Acc. Chem. Res.* **2013**, *46*, 1252−1260.
(9) Luque, A.; Marti, A.; Nozik, A. J. Solar Cells Based on Quantum Dots: Multiple Exciton Generation and Intermediate Bands. *MRS Bull.* **2007**, *32*, 236−241.
(10) Hu, J.; Odom, T. W.; Lieber, C. M. Chemistry and Physics in One Dimension: Synthesis and Properties of Nanowires and Nanotubes. *Acc. Chem. Res.* **1999**, *32*, 435−445.
(11) Huang, Y.; Lieber, C. M. Integrated Nanoscale Electronics and Optoelectronics: Exploring Nanoscale Science and Technology Through Semiconductor Nanowires. *Pure Appl. Chem.* **2004**, *76*, 2051−2068.
(12) Nozik, A. J.; Beard, M. C.; Luther, J. M.; Law, M.; Ellingson, R. J.; Johnson, J. C. Semiconductor Quantum Dots and Quantum Dot Arrays and Applications of Multiple Exciton Generation to Third-Generation Photovoltaic Solar Cells. *Chem. Rev.* **2010**, *110*, 6873−6890.
(13) Liu, Z.; Sun, Y.; Yuan, J.; Wei, H.; Huang, X.; Han, L.; Wang, W.; Wang, H.; Ma, W. High-Efficiency Hybrid Solar Cells Based on Polymer/PbSxSe1-x Nanocrystals Benefiting from Vertical Phase Segregation. *Adv. Mater.* **2013**, *25*, 5772−5778.
(14) Kramer, I. J.; Sargent, E. H. Colloidal Quantum Dot Photovoltaics: A Path Forward. *ACS Nano* **2011**, *5*, 8506−8514.
(15) Barkhouse, D. A. R.; Pattantyus-Abraham, A. G.; Levina, L.; Sargent, E. H. Thiols Passivate Recombination Centers in Colloidal Quantum Dots Leading to Enhanced Photovoltaic Device Efficiency. *ACS Nano* **2008**, *2*, 2356−2362.
(16) Etgar, L.; Park, J. H.; Barolo, C.; Nazeeruddin, M. K.; Viscardi, G.; Graetzel, M. Design and Development of Novel Linker for PbS Quantum Dots /TiO_2 Mesoscopic Solar cell. *ACS Appl. Mater. Interfaces* **2011**, *3*, 3264−3267.
(17) Giansante, C.; Carbone, L.; Giannini, C.; Altamura, D.; Ameer, Z.; Maruccio, G.; Loiudice, A.; Belviso, M. R.; Cozzoli, P. D.; Rizzo, A.; Gigli, G. Colloidal Arenethiolate-Capped PbS Quantum Dots: Optoelectronic Properties, Self-Assembly, and Application in Solution-Cast Photovoltaics. *J. Phys. Chem. C* **2013**, *117*, 13305−13317.
(18) Aaron, D.; Barkhouse, R.; Debnath, R.; Kramer, I. J.; Zhitomirsky, D.; Pattantyus-Abraham, A. G.; Levina, L.; Etgar, L.; Grätzel, M.; Sargent, E. H. Depleted Bulk Heterojunction Colloidal Quantum Dot Photovoltaics. *Adv. Mater.* **2011**, *23*, 3134−3138.
(19) Lan, X.; Bai, J.; Masala, S.; Thon, S. M.; Ren, Y.; Kramer, I. J.; Hoogland, S.; Simchi, A.; Koleilat, G. I.; Paz-Soldan, D.; et al. Self-Assembled, Nanowire Network Electrodes for Depleted Bulk Heterojunction Solar Cells. *Adv. Mater.* **2013**, *25*, 1769−1773.
(20) Kramer, I. L.; Zhitomirsky, D.; Bass, J. D.; Rice, P. M.; Topuria, T.; Krupp, L.; Thon, S. M.; Ip, A. H.; Debnath, R.; Kim, H.-O.; Sargent, E. H. Ordered Nanopillar Structured Electrodes for Depleted Bulk Heterojunction Colloidal Quantum Dot Solar Cells. *Adv. Mater.* **2012**, *24*, 2315−2319.
(21) Yu, G.; Gao, J.; Hummelen, J. C.; Wudl, F.; Heeger, A. J. Polymer Photovoltaic Cells: Enhanced Efficiencies via a Network of Internal Donor-Acceptor Heterojunctions. *Science* **1995**, *270*, 1789−1791.
(22) Osterhout, S. D.; Wienk, M. M.; Van Bavel, S. S.; Thiedmann, R.; Koster, L. J. A.; Gilot, J.; Loos, J.; Schmidt, V.; Janssen, R. A. J. The Effect of Three-Dimensional Morphology on the Efficiency of Hybrid Polymer Solar Cells. *Nat. Mater.* **2009**, *8*, 818−824.
(23) Kemp, K. W.; Labelle, A. J.; Thon, S. M.; Ip, A. H.; Kramer, I. J.; Hoogland, S.; Sargent, E. H. Interface Recombination in Depleted Heterojunction Photovoltaics Based on Colloidal Quantum Dots. *Adv. Energy Mater.* **2013**, *3*, 917−922.
(24) Hyun, B.-R.; Choi, J. J.; Seyler, K. L.; Hanrath, T.; Wise, F. W. Heterojunction PbS Nanocrystal Solar Cells with Oxide Charge-Transport Layers. *ACS Nano* **2013**, *7*, 10938−10947.
(25) Loiudice, A.; Rizzo, A.; De Marco, L.; Belviso, M. R.; Caputo, G.; Cozzoli, P. D.; Gigli, G. Organic Photovoltaic Devices with Colloidal TiO_2 Nanorods as Key Functional Components. *Phys. Chem. Chem. Phys.* **2012**, *14*, 3987−3995.
(26) Loiudice, A.; Rizzo, A.; Grancini, G.; Belviso, M. R.; Corricelli, M.; Curri, M. L.; Striccoli, M.; Agostiano, A.; Cozzoli, P. D.; Petrozza, A.; Lanzani, G.; Gigli, G. Fabrication of Flexible All-Inorganic Nanocrystal Solar Cells by Room-Temperature Processing. *Energy Environ. Sci.* **2013**, *6*, 1565−1572.
(27) Buonsanti, R.; Carlino, E.; Giannini, C.; Altamura, D.; De Marco, L.; Giannuzzi, R.; Manca, M.; Gigli, G.; Cozzoli, P. D. Hyperbranched Anatase TiO_2 Nanocrystals: Nonaqueous Synthesis, Growth Mechanism, and Exploitation in Dye-Sensitized Solar Cells. *J. Am. Chem. Soc.* **2011**, *133*, 19216−19239.
(28) Miszta, K.; de Graaf, J.; Bertoni, G.; Dorfs, D.; Brescia, R.; Marras, S.; Ceseracciu, L.; Cingolani, R.; van Roij, R.; Dijkstra, M.; Manna, L. Hierarchical Self-Assembly of Suspended Branched Colloidal Nanocrystals into Superlattice Structures. *Nat. Mater.* **2011**, *10*, 872−876.
(29) Vanmaekelbergh, D. Self-Assembly of Colloidal Nanocrystals as Route to Novel Classes of Nanostructured Materials. *Nano Today* **2011**, *6*, 419−437.
(30) De Marco, L.; Manca, M.; Giannuzzi, R.; Belviso, M. R.; Cozzoli, P. D.; Gigli, G. Shape-Tailored TiO_2 Nanocrystals with Synergic Peculiarities as Building Blocks for Highly Efficient Multi-Stack Dye Solar Cells. *Energy Environ. Sci.* **2013**, *6*, 1791−1795.
(31) Dayal, S.; Reese, M. O.; Ferguson, A. J.; Ginley, D. S.; Rumbles, G.; Kopidakis, N. The Effect of Nanoparticle Shape on the Photocarrier Dynamics and Photovoltaic Device Performance of Poly(3-hexylthiophene):CdSe Nanoparticle Bulk Heterojunction Solar Cells. *Adv. Funct. Mater.* **2010**, *20*, 2629−2635.